

Chapter 10

Synthesis and Physical Properties

Characterization of CdSe_{1-y}S_y Nanolayers Deposited by Chemical Bath Deposition at Low-Temperature Treatment

J.E. Flores-Mena, J.I. Contreras-Rascón, J. Diaz-Reyes,
and R.S. Castillo-Ojeda

Abstract In this work, we present the synthesis and structural and optical characterizations of CdSe_{1-y}S_y deposited by chemical bath deposition (CBD) technique on corning glass at a temperature of 20 ± 2 °C. The sulfur molar fraction was varied from 0 to 42.13 %, which was realized by varying the thiourea volume added to the growth solution in the range from 0 to 30 mL. The chemical stoichiometry was estimated by energy dispersive spectrometry (EDS). The CdSe_{1-y}S_y showed hexagonal wurtzite crystalline phase that was found by X-ray diffraction (XRD) analysis and Raman spectroscopy. The average grain size range of the films was 1.48–1.68 nm that was determined using the Debye–Scherrer equation W(002) direction and was confirmed by high-resolution transmission electron microscopy (HRTEM). Raman scattering shows that the lattice dynamics is characteristic of bimodal behavior and the multipeaks adjust to the first optical longitudinal mode for the CdSeS, in all cases, Raman spectra show two dominant vibrational bands about 208 and 415 cm⁻¹ associated at CdSe-1LO-like and CdSe-2LO-like. CdSe_{1-y}S_y band gap energy can be varied from 1.86 to 2.16 eV by varying the thiourea volume added in growth solution in the investigated range obtained by transmittance

J.E. Flores-Mena

Benemérita Universidad Autónoma de Puebla, Facultad de Ciencias de la Electrónica, Av. San Claudio y 18 sur, Ciudad Universitaria, Puebla, Puebla 72500, Mexico

J.I. Contreras-Rascón

Universidad de Sonora, División de Ciencias Exactas y Naturales, Col. Centro, Hermosillo, Sonora 83000, Mexico

J. Diaz-Reyes (✉)

Instituto Politécnico Nacional, Centro de Investigación en Biotecnología Aplicada, Ex-Hacienda de San Juan Molino Km 1.5, Tepetitla, Tlaxcala 90700, Mexico
e-mail: joel_diaz_reyes@hotmail.com

R.S. Castillo-Ojeda

Universidad Politécnica de Pachuca, Km. 20, Rancho Luna, Ex-Hacienda de Sta. Bárbara, Zempoala, Hidalgo 43830, Mexico

measurements at room temperature. The room temperature photoluminescence shows a dominant radiation band at about 3.0 eV that can be associated with exciton bonded to donor impurity and the quantum confinement because of the grain size is less than the Bohr radius.

Keywords CBD • HRTEM • X-ray diffraction • Photoluminescence • Raman spectroscopy

10.1 Introduction

The development of next-generation solar cells including sensitized inks solar cells (dye solar cells), that make use of the concept of the intermediate band cells and nanostructures, exceed the limit Shockley–Queisser efficiency for a single absorption, 31 %, this is one of the most fascinating challenges in research on sustainable energy. In this regard, semiconductor quantum dots (QDs) have shown properties very attractive for the development of solar cells that exceed the current limitations. The demonstration of efficient processes, multiple exciton generation (MEG) in colloidal quantum dots, has aroused great interest in the use of these materials in photovoltaic devices. In particular, the mixed semiconductor $\text{CdSe}_{1-y}\text{S}_y$ in semiconductor quantum dot technology from binary materials, cadmium sulfide (CdS) and cadmium selenide (CdSe). The cadmium chalcogenide $\text{CdSe}_{1-y}\text{S}_y$ semiconducting alloy is characterized by a variable direct band gap which can be tuned by alloying, from 1.72 eV for CdSe to 2.44 eV for CdS at room temperature. Because of excellent properties of Cd(S,Se), it is used in optoelectronic devices, photoconductors, gamma ray detectors, visible-light emitting diodes, lasers and solar, cells [1]; and the references cited therein. $\text{CdSe}_{1-y}\text{S}_y$ solid solutions have attracted great interest in recent years from both experimental and theoretical points of view [1, 2].

The CdS known as material optical window also acts as a passivating agent which forms an enveloping film relatively inert on the absorbent material (CdSe), which masks against the action of external agents. Although the reaction between the material and the external agent is thermodynamically feasible macroscopically, the layer or passivation film does not allow them to interact. There have been many efforts to find better agents that allow to passivate the surface of the nanoparticle, such as thiourea organic agent [3]. This mixed semiconductor offers one of the best alternatives for the performance of photovoltaic devices. Expectations for the semiconductor solar cell $\text{CdSe}_{1-y}\text{S}_y$ with an irradiance of 100 mW/cm^2 are: current density (J_{sc}) estimated at 29 mA/cm^2 [4], open circuit voltage estimated at 1.0 V [4], and an expected quantum efficiency at 17.5 % [5, 6].

Deposition by chemical bath technique of thin films consists of moderate release of metal ions into alkaline solution [7]. This technique has become important for the development of thin film solar cells, since the synthesis of CdS by this method offers a better efficiency than traditional evaporation method [8–10]. In the formation of

the film exhibit two different mechanisms: The first mechanism is that involving the reaction of atomic species on the surface, this mechanism is called ion-to-ion [11–13]. The second mechanism is associated with the agglomeration of colloids formed in the solution, which can be regarded as an increase in grouping or cluster by cluster. For practical purposes, the formation of the core, which leads to the formation of the film, can occur by a process of heterogeneous nucleation on the substrate or through a process of homogeneous nucleation in the volume of the solution.

In this work we report the synthesis and characterization of CdSe_{1-y}S_y nanocrystals in one step by chemical bath deposition on glass substrate at low temperature. In particular, the effects of the chemical composition on structural and optical properties of the CdSe_{1-y}S_y alloy were studied by X-ray diffraction, HRTEM, EDS, Raman scattering, transmittance, and photoluminescence (PL).

10.2 Experimental

CdSe_{1-y}S_y was deposited by chemical bath deposition (CBD), technique which requires no a special growth atmosphere, the used deposition temperature is low. With this technique it is possible to obtain large areas of film, thickness control, and also highly reproducible results [14]. The growth technique requires during the reactions: control of physical and chemical parameters such as mechanical stirring, temperature, concentration of chemical reagents, pH, and adequate volume ratio. With these experimental conditions it is possible to obtain polycrystalline thin films on different substrate types. The feasibility of this technique for its environment is: deposit short time, it does not require high temperatures, there is no emission of toxic gases and the preparation of the solutions is carried out on micro scale. The nanofilms were deposited on substrates of corning glass at a temperature (T_d) of $20 \pm 2^\circ\text{C}$ and the deposit time was 30 min. Deionized water of $20\text{ M}\Omega\text{-cm}$ was utilized to prepare the aqueous solutions that are composed by CdCl₂ [0.01 M], KOH [0.1 M], SeC(NH₂)₂ [0.1 M], and NH₄NO₃ [0.1 M]. Systematically, it was adding thiourea (SC(NH₂)₂) [0.2 M]. The selenourea (SeC(NH₂)₂) solution was prepared in an argon inert atmosphere, because it is unstable under laboratory conditions and should be maintained at a temperature of 4°C to avoid chemical decomposition. For carrying out the intentional doping by sulfur of the deposited layers are added small thiourea volumes to the growth solution in the range of 0 to 30 mL to obtain different sulfur concentrations in the nanostructures, which are presented in Table 10.1. The Cd, Se, and S concentrations in CdSe_{1-y}S_y samples were estimated by means of energy dispersive spectroscopy (EDS).

The CdSe_{1-y}S_y films chemical stoichiometry was obtained by energy dispersive spectrometry (EDS) that was carried out in a System LEO 438VP, with W.D. of 26 mm using a pressure of 20 Pa. The crystalline phase and structure of the films were determined with a Bruker D8 Discover diffractometer using the copper K α radiation ($\lambda = 1.5406 \text{ \AA}$) at 40 kV and 40 mA with parallel beam geometry.

Table 10.1 Summary of the CdSe_{1-y}S_y samples grown and studied in this work and the doping volume added to each one

Sample	SC(NH ₂) ₂ added volume (mL)	Cd molar fraction	Se molar fraction	S molar fraction
M100	00	49.11	50.89	0.00
M205	05	56.40	26.96	16.64
M310	10	57.76	20.20	22.08
M415	15	55.54	18.23	26.23
M520	20	53.76	12.62	33.62
M625	25	55.76	4.46	39.78
M730	30	55.48	2.39	42.13

High-resolution transmission electron microscopy (HRTEM) studies were carried out in a JEOL JEM200 of 80–200 kV, the obtained image is recorded with a CCD camera in real time. The Gatan Digital Micrograph software was used for the analysis of HRTEM images. Raman scattering experiments were performed at room temperature using the 6328 Å line of a He–Ne laser at normal incidence for excitation. The light was focused to a diameter of 6.0 μm on the sample using a 50× (numerical aperture 0.9) microscope objective. The nominal laser power used in these measurements was 20 mW. Scattered light was analyzed using a micro-Raman System (Labram model of Dilor), a holographic notch filter made by Kaiser Optical System, Inc. (model superNotch-Plus), a 256 × 1024-pixel CCD used as detector cooled to 140 K using liquid nitrogen, and two interchangeable gratings (600 and 1800 g/mm). Typical spectrum acquisition time was limited to 60 s to minimize the sample heating. Room temperature photoluminescence was taken with a solid-state laser (325 nm) with 60 mW as excitation source and a SCIENCETECH 9040 monochromator was used to perform the sweep of wavelength at room and low temperature in a CRYOGENICS cryostat.

10.3 Results and Discussion

10.3.1 X-ray Microanalysis (EDS)

The chemical composition of the CdSe_{1-y}S_y samples was estimated by EDS, which besides allows to know the presence of any unintentional impurities. Figure 10.1 shows the EDS spectra of typical samples, M100 and M730, which indicate the presence of oxygen in the samples along with cadmium, selenium, and sulfur.

The EDS spectra indicate that besides Cd, Se, and S, the samples contain a significant amount of silicon, potassium, calcium, sodium, and oxygen, and other residual impurities, which come from the substrate. By XPS analysis, in other materials such as ZnS, it has been showed that oxygen ions are present in the

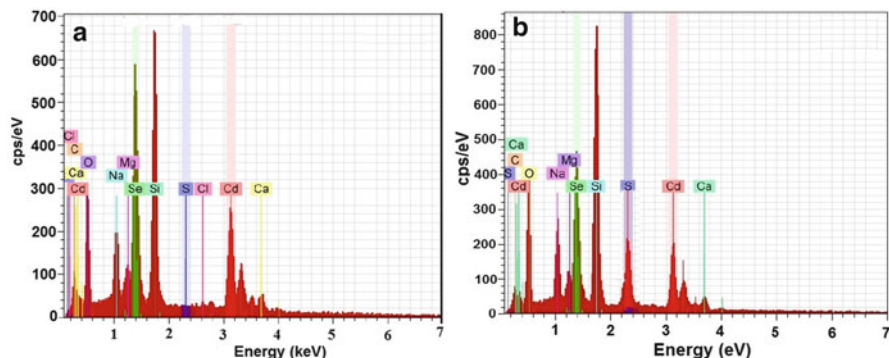


Fig. 10.1 EDS spectra of two CdSeS typical samples, M100 and M730. The spectra indicate that the samples contain a significant amount of residual impurities come from the substrate

samples in the form of O^{2-} ions that may produce CdO in the sample [15]. Since the temperature during synthesis and air drying in the present case is low, this conversion may have happened only at a very low percentage so that the presence of CdO could not be detected by XRD measurements, as will be seen below. However, these oxygen ions can form trap levels in the band gap, resulting in several transitions contributing to luminescence. Thus, it appears that oxygen has replaced sulfur or selenium at a few random points of the CdSeS lattice. The results of such measurements for the cadmium, selenium, and sulfur are shown in Table 10.1. From these results it is observed that the samples do not have a good stoichiometry and that they have a greater presence of cadmium in the material and an absence of sulfur and selenium. Considering that each unit cell contains two Cd atoms and two sulfur and selenium atoms, then when a stoichiometric deviation of ideal unit cell occurs it could establish a correspondence between vacancies or interstices of some of the elements (V_{Cd} , V_{Se} , V_S , Cd_i , Se_i , S_i). From Table 10.1 one can observe that the samples contain lower sulfur and selenium concentrations, which indicate that they have a higher structural defects concentration as is this case of the present work, where there are excess of II element and lack of VI elements.

10.3.2 X-ray Diffraction

Figure 10.2a shows the XRD diffractograms of the CdSe_{1-y}S_y nanostructures deposited with different sulfur molar fractions, which have similar diffractograms. Figure 10.2b shows the deconvolution into individual components (Gaussian shape) of two typical polycrystalline films that are the extreme cases for sulfur molar fractions, M100 and M730 samples, which present five peaks that will be discussed below. It is observed from XRD patterns that CdSe_{1-y}S_y deposited films are in nature polycrystalline whose crystalline phase is hexagonal wurtzite, which shows

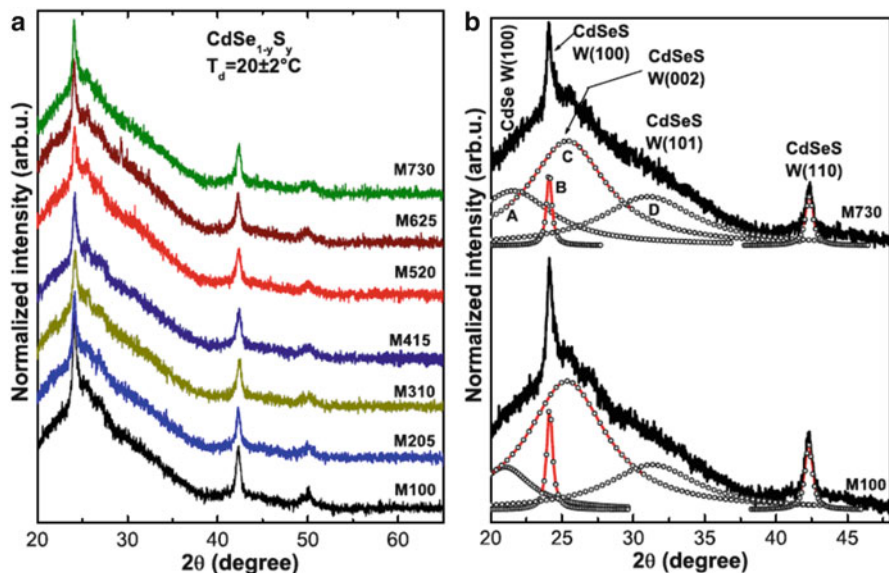


Fig. 10.2 (a) X-ray patterns of $\text{CdSe}_{1-y}\text{S}_y$ nanofilms with different S concentrations. (b) It shows the deconvolution of X-ray diffractograms of two typical samples: M100 and M730

a preferential growth in the (002) direction, besides there are other important peaks in the (110) and (112) directions. The X-ray patterns of deposited $\text{CdSe}_{1-y}\text{S}_y$ thin films are described in the $P63mc$ (186) and whose lattice parameters were calculated using the software DICVOL04, obtaining the following average lattice constant values CdSe : $a = 4.178 \text{ \AA}$ and $c = 6.972 \text{ \AA}$, which are in agreement with the reported values [16, 17].

All of the products displayed the XRD peaks corresponding to wurtzite (JCPDS-ICDD X-ray diffraction cards numbers 19-191 and 8-459, for cubic and hexagonal phases of CdSe , respectively) and no characteristic diffraction peaks arising from the possible impurity phases such as S and CdO were observed, indicating the preparation of pure wurtzite samples. In all cases the diffractograms present the same X-ray diffractions and some of them can be assigned as shown in Fig. 10.2b.

Besides, it is observed a widening at the peak of the preferential W(002) direction, which could be caused by undergoing stress, size of small crystalline domain, or fluctuations in concentration. The first case does not happen since the used substrates are amorphous and they do not produce a mismatch in the lattice constants. The variation in the size of the average domain crystalline is responsible for this widening. The mean grain size was calculated from hexagonal wurtzite (002) diffraction of $\text{CdSe}_{1-y}\text{S}_y$ for all the studied samples, which are shown in Table 10.2. Figure 10.2b shows the deconvolution of X-ray diffractograms of the samples M100 and M730 that were deposited with 0 and 30 mL of thiourea in the growth solution. The crystallite sizes ($D_{(hkl)}$) were calculated from the line broadening of the X-ray

Table 10.2 Mean grain sizes of the nanostructures obtained by Debye–Scherrer equation and the distance interplanar and optical band gap energies obtained by transmittance

Sample	a (Å)	c (Å)	$d_{(002)}$ (Å)	$d_{(100)}$ (Å)	Grain Size (nm)	Band gap (eV)
M100	4.173	6.971	3.510	3.720	1.48	1.87
M205	4.195	6.983	3.438	3.661	1.21	2.05
M310	4.191	7.025	3.501	3.708	1.20	1.91
M415	4.120	6.942	3.485	3.690	1.41	1.89
M520	4.172	6.776	3.469	3.708	1.68	1.89
M625	4.186	6.773	3.469	3.672	1.56	2.06
M730	4.134	6.801	3.485	3.708	1.59	2.16

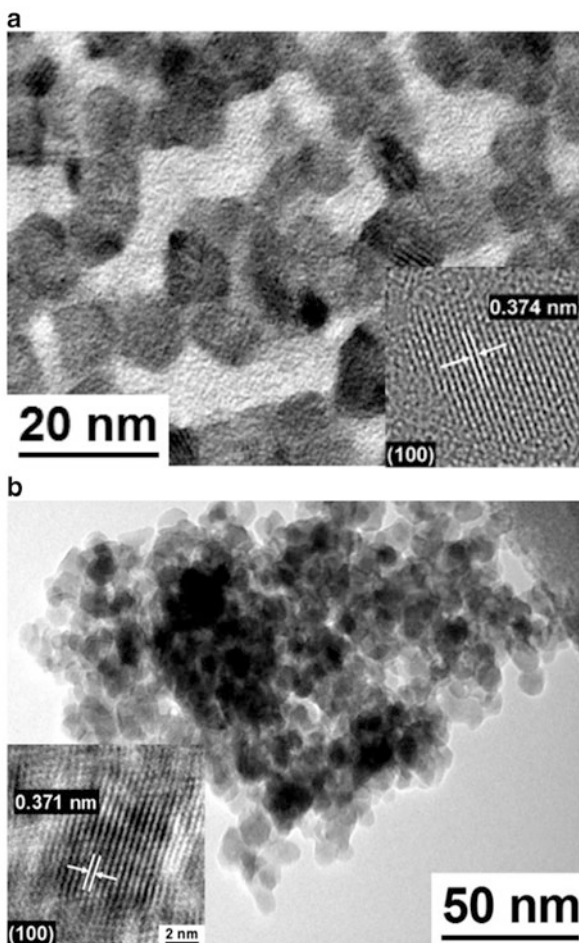
diffraction peaks at 2θ using the Debye–Scherrer equation, $D_{(hkl)} = n\lambda/\beta \cos \theta$ [18, 19]. In a tetragonal structure, there are two parameters, $a = b$ and c , that have to be calculated. The lattice parameters of CdSe_{1-y}S_y and the grain sizes calculated using the Debye–Scherrer equation are presented in Table 10.2. As is observed in Table 10.2, as shown in Table 10.2, there is little variation in the grain size despite the wide variation in the S mole fraction, having an average grain size of 1.41 nm for the first five samples and the last two are increased slightly. These values indicate that there is a high quantum confinement because the grain sizes are smaller than the Bohr radii of binary compounds, Bohr radii of CdS (2.8 nm) and CdSe (4.9 nm). Table 10.2 shows the mean grain sizes of the nanostructures obtained by the Debye–Scherrer equation for the direction W(002), which shows the dependence of the grain size of the average crystalline domain based on the increase of sulfur molar fraction for the CdSe_{1-y}S_y system. Additionally, it is shown the distance interplanar and optical band gap energies obtained by transmittance.

10.3.3 High-Resolution Transmission Electron Microscopy

Figure 10.3 illustrates the images obtained by high-resolution transmission electron microscopy (HRTEM) for two typical samples, M625 and M730, and insets are the results of the processing of the HRTEM images using filters in Fourier space. There is a crystal structure of nearly spherical shape of the material with an average size of 6.3 and 7.16 nm, in addition in the insets can see clearly the distance interplanar of material, about 0.371 nm, which corresponds to the direction of the hexagonal phase of the CdSeS (100).

As can be seen, the results obtained by HRTEM are in good agreement with the results calculated from X-ray diffraction for grain size and interplanar distance and the differences are due to the used approximations and the equipment limitations.

Fig. 10.3 HRTEM micrographs of typical CdSe_yS_{1-y} samples for two: (a) M625 and (b) M730



10.3.4 Raman Spectroscopy

Back scattering geometry has been used to record the Raman spectra of all CdSe_{1-y}S_y samples, which are shown in Fig. 10.4. As can be observed in figure all Raman spectra are similar, i.e., the Raman spectra do not depend strongly on the sulfur concentration in the layer. Figure 10.5 shows the Raman spectra of three samples: M100, M205, and M730, which were grown with zero, the lower and higher thiourea volume in the growth solution. Raman spectrum of the sample M730 features an asymmetric fundamental Raman band at around 208 cm⁻¹. The spectrum can be deconvoluted in six Lorentzian line shape signals, which are observed at 187, 209, 272, 377, 417, and 601 cm⁻¹. The dominant mode at 209 cm⁻¹ is observed nearly at frequency of 1LO-CdSe, see Fig. 10.5a, by which is associated to the first order CdSe longitudinal optical phonon like (CdSe-1LO-like) in hexagonal wurtzite

Fig. 10.4 Raman spectra of the $\text{CdSe}_{1-y}\text{S}_y$ films by adding different sulfur volumes deposited at the temperature of $20 \pm 2^\circ\text{C}$

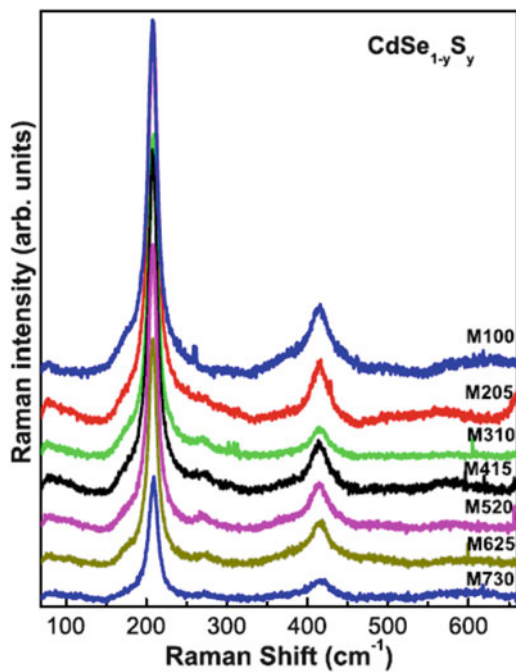
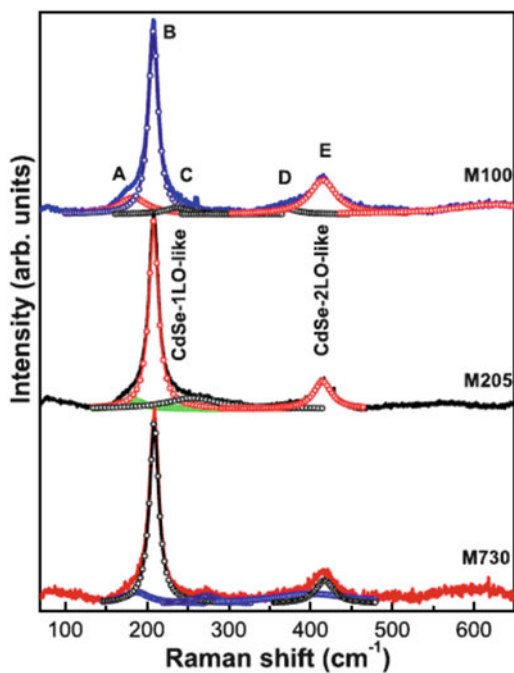


Fig. 10.5 Decomposition of the Raman spectra into individual components for three samples: (a) M100, (b) M205, and (c) M730. The dashed lines are their respective fitting

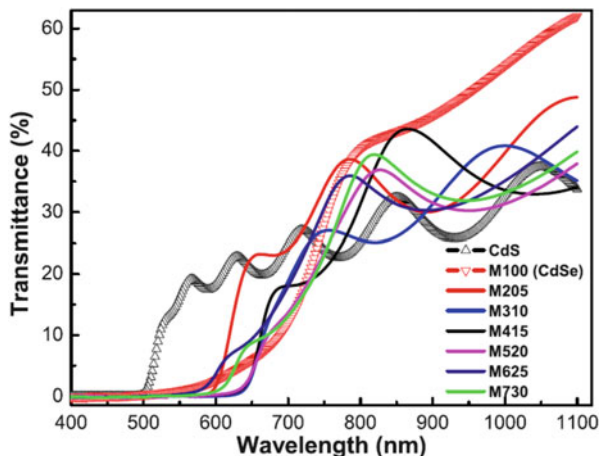


phase [16, 20]. In the same way, the Raman mode corresponding to the low-energy shoulder (187 cm^{-1}) originates from surface optical phonon modes (SO) [21, 22]. The feature at the high-energy shoulder, observed at 272 cm^{-1} , is the subject of a recent study by Dzhagan et al. [23], who suggest that it is resulted from the participation of acoustic phonons to the scattering process but is notorious for its Raman shift at higher frequencies. The Raman band at 417 cm^{-1} is associated with the second longitudinal optical mode like of the CdSe (CdSe-2LO-like) [16]. On the other hand, the bands observed around 400 and 600 cm^{-1} are overtones of the fundamental Raman band. Finally, the modes observed at 377 and 601 cm^{-1} correspond to the second and third phononic replica of the SO mode, 2SO and 3SO, respectively. The Raman intensity of the CdSe-1LO-like and CdSe-2LO-like bands decreases with the increase of thiourea compound concentration in growth solution, as can see in Fig. 10.5. From Fig. 10.5 it is observed that the CdSe-1LO-like Raman line is not only broadened, but it also shows an asymmetric broadening towards the low frequency side. Besides, the frequency of the 1LO-like peaks does not undergo any Raman shift by the thiourea volume increase in the samples but their FWHMs have decreased noticeably compared to that of the M205 (M100) sample FWHM. It is now well known that confinement of phonons, optical as well as acoustic, influences the phonon spectra conspicuously when the grain size falls to a few nanometers. Confinement of optical phonons causes an asymmetry in the line shape and a shift towards the low frequency side compared to that for bulk CdSe.

10.3.5 Transmittance

The transmittance spectra in the visible and infrared ranges are recorded for the $\text{CdSe}_{1-y}\text{S}_y$ films in the wavelength range of $400\text{--}1100\text{ nm}$, which were measured at room temperature. The effect of sulfur added in the nanolayers on the optical properties including percentage of transmittance (% of T) and band gap energy (E_G) was studied in detail. The transmittance observed of the CdSe film in the visible range varies from about 0 up to nearly 60% (without considering the substrate contribution) and it is higher of all shown transmittance spectra. The sharp reduction in the transmittance spectra at the wavelengths lower than 600 nm is due to the fundamental absorption edges of the different films. The $\text{CdSe}_{1-y}\text{S}_y$ transmittance decreases lightly as the sulfur molar fraction is increased, see Fig. 10.6. This causes the slight blue shift in optical band gap energy, which confirms the formation of $\text{CdSe}_{1-y}\text{S}_y$ with increasing y . It is observed from the transmittance spectra that the absorption edges are also slightly shifted towards the higher energy region for the films with higher sulfur molar fraction. The optical band gap (E_G) of a semiconductor is related to the optical absorption coefficient (α) and the incident photon energy ($h\nu$). The absorption coefficient α for a film of thickness d and reflectance R is determined near the absorption edge using the simple relation: $\alpha = \ln \left\{ (1 - R)^2 / T + \left[((1 - R^2) / 2T)^2 + R^2 \right]^{1/2} \right\} / d$, where multiple reflections are

Fig. 10.6 Transmittance spectra of CdSe_{1-y}S_y nanofilms measured at room temperature



taken into, but interference neglected. Actually a transmission interference pattern could be observed in most samples, and was used to obtain an accurate value for the thickness d . The optical band gap of CdSeS has been evaluated from the transmittance spectrum using the Tauc relation [18, 19, 24]: $\alpha hv = (E_G - hv)^n$, where n depends on the kind of optical transition that prevails. Specifically, n is $1/2$ and 2 when the transition is directly and indirectly allowed, respectively. The CdSeS film is known to be a semiconductor with a directly allowed transition, therefore $n = 1/2$. The CdSe_{1-y}S_y average band gaps, which were estimated from the linear portion of the $(\alpha hv)^2$ vs hv (see inset of Fig. 10.7), are shown in Table 10.2 and Fig. 10.7. The band gap energies were higher than the value of bulk wurtzite CdSe (1.74 eV) [25] due to quantum confinement of CdSe nanocrystals. The optical band gap of the CdSe film is of 1.86 eV that corresponds to pure CdSe and is 140 meV higher than band gap in CdSe bulk. This discrepancy is associated with the average grain size [19, 24]. For sample M730 its optical bandgap is increased slightly about 300 meV compared to the bandgap of the sample M100, which can be related to sulfur incorporation to the molecule and the average grain size, as can see in Fig. 10.7. This band gap increase can be explained due to the substitution in the lattice of selenium atoms (ionic radii ~ 1.98 Å) by sulfur atoms that are smaller (ionic radii ~ 1.84 Å).

10.3.6 Room Temperature Photoluminescence

Figure 10.8 illustrates the room temperature photoluminescence spectra of the CdSe_{1-y}S_y films studied. Figure 10.9 shows the room temperature photoluminescence spectra of three typical CdSe_{1-y}S_y samples: M100, M205, and M730. The photoluminescence spectrum of the M100 sample shows two dominant broad bands,

Fig. 10.7 It shows the band gap energy as a function of the sulfur molar fraction. The inset shows Tauc plot of CdSeS samples to two different molar fractions: (a) $x = 21.54\%$ and (b) $x = 100\%$

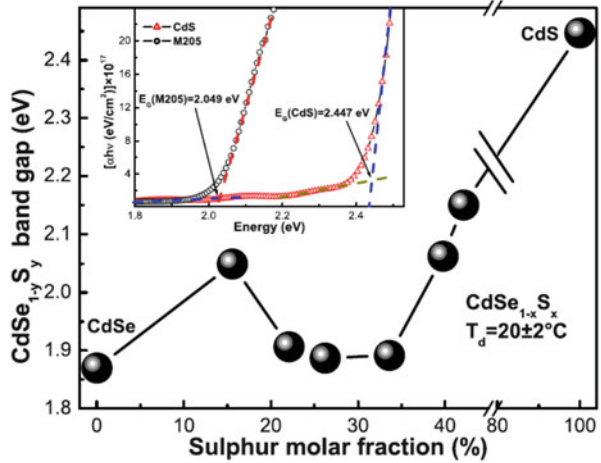
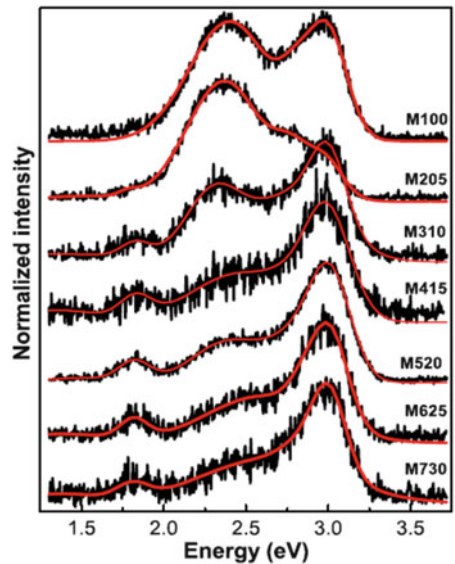
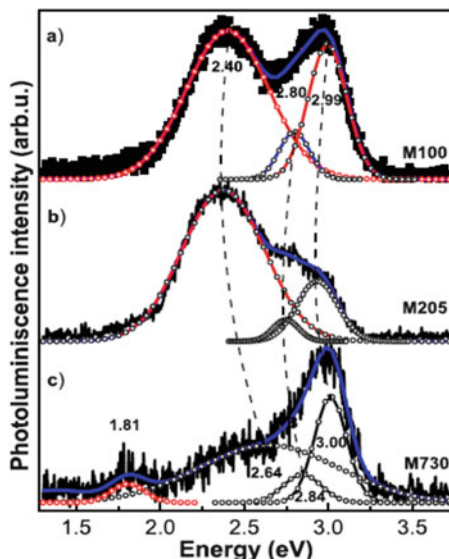


Fig. 10.8 It illustrates the room temperature photoluminescence spectra of the $\text{CdSe}_{1-y}\text{S}_y$ samples grown with different S molar fractions



which through a standard fitting procedure performed in the interval 1.3–3.75 eV, such bands can be deconvoluted in three Gaussian line shape signals as are shown in Fig. 10.9 observed at 2.99, 2.80, and 2.40 eV. As is observed in Figs. 10.8 and 10.9 the radiative bands depend strongly on the sulfur concentrations incorporated in the layers. The main radiative band at 3.00 eV is associated with an exciton bound to a donor level [26]. The others are wide bands, observed in the violet, blue, and red regions of the visible spectrum at 2.80 and 2.40 eV and are associated with emissions due to impurity levels. The broad bands indicate that these defect-related luminescence peaks are caused by radiative transitions between selenium (sulfur) vacancies or Cd interstitials acting as shallow donors and Cd vacancies

Fig. 10.9 Deconvolution of the photoluminescence spectra into individual components for three sulfur molar fractions. The *dashed lines* are merit-figures to follow the behavior of the radiative bands



acting as deep acceptors. This recombination mechanism competes with the exciton-related luminescence and seems to depend on the stoichiometry and the preparation conditions of the CdSe films rather than on their microstructure [27, 28] as is shown in Fig. 10.9. Starting from the photoluminescence spectrum of the M100 sample (CdSe), which shows that the main radiation bands depend strongly on the sulfur molar fraction in the layers, because with its increase excitonic band becomes dominant and shifts slightly at higher energies. Violet emission observed at 2.80 eV for low molar fraction shifted at 2.84 eV for high molar fraction and the green band at 2.40 eV is displaced to blue by 24 meV. Finally, the red emission band at 1.81 eV shifted to blue with increase of sulfur molar fraction in layers. As is observed in Fig. 10.7, the band gap energy of CdSe_{1-y}S_y is between 1.86 and 2.16 eV, and radiative transitions are observed at higher energies, therefore these are associated with the grain size and the quantum confinement. The band gap values were higher than the value of bulk CdSe_{1-y}S_y due to quantum confinement of CdSe_{1-y}S_y nanocrystals [19]. As is observed in Fig. 10.8, excitonic band is lightly blue shifted for all samples. This phenomenon was likely due to the quantum confinement effect of the CdSeS nanocrystals [29], whose diameters are several nanometers,

This quantum confinement effect can be clearly explained using the particle energy relation of the three dimensional single-particle box [24]: $E = D(n_x^2/x^2 + n_y^2/y^2 + n_z^2/z^2)$, where D is a constant; n_x , n_y , n_z are the quantum number and x , y , z are the scales in each dimension. Apparently, a decreased x , y , z values (the diameters of CdSe_{1-y}S_y particles) leads to an increased energy E . The reduction of diameters of the particles produces a blue shift of the band edge. This is a good demonstration of the quantum confinement effect in the nanoparticles

and other 0D nanostructure [30, 31]. Hence, it is critically important to synthesize the $\text{CdSe}_{1-y}\text{S}_y$ nanoparticles of a size comparable with Bohr radius and of a narrow size distribution in order to ensure the occurrence of the quantum confinement [31]. Cadmium selenium has a low exciton Bohr radius (4.9 nm) and cadmium sulfide has a low exciton Bohr radius (2.8 nm). These values are comparable to grain size of the nanoparticles, whose values were estimated by X-ray diffraction.

10.4 Conclusions

Heat-treating an API 5L X-65 pipe steel to 1050 °C for 30 min following water cooling yields an acicular ferrite microstructure with a mechanical strength 200 MPa larger than the as-received steel. Although hardness also increases, the average value is below the recommended to avoid susceptibility to SSC. The results obtained with the non-conventional heat treatment yield similar properties to an API 5L X-80 steel, however the high hardness of this steel prevents its use with sour hydrocarbons. The findings of this study imply that it is possible to reduce the wall thickness of pipelines to transport crude oil while maintaining its resistance to SSC.

Acknowledgements The authors would like to thank CONACYT for financial support and the IIM-UMSNH for technical support.

References

1. Xu F, Ma X, Kauzlarich SM, Navrotsky A (2009) Enthalpies of formation of $\text{CdS}_x\text{Se}_{1-x}$ solid solutions. *J Mater Res* 24:1368–1374
2. Mujica A, Rubio A, Muñoz A, Needs RJ (2003) High-pressure phases of group-IV, III–V, and II–VI compounds. *Rev Mod Phys* 75:863–912
3. Pattabi M, Uchil J (2000) Synthesis of cadmium sulphide nanoparticles. *Sol Energy Mater Sol Cell* 63:309–314
4. Ullal HS, Stone JL, Zweibel K, Surek T, Mitchell RL (1992) Polycrystalline thin-film solar cells and modules. In: 6th International photovoltaic science & engineering conference, New Delhi, India 10–14 February 1992
5. Morales-Acevedo A (2006) Can we improve the record efficiency of CdS/CdTe solar cells? *Sol Energy Mater Sol Cells* 90:2213–2220
6. Gordillo G (1995) Preparation and characterization of CdTe thin films deposited by CSS. *Sol Energy Mater Sol Cells* 37:273–281
7. Switzer JA, Hodes G (2010) Electrodeposition and chemical bath deposition of functional nanomaterials. *MRS Bull* 35:743–749
8. Kozhevnikova NS, Vorokh AS, Uritskaya AA (2015) Cadmium sulfide nanoparticles prepared by chemical bath deposition. *Russ Chem Rev* 84:225–250
9. Hodes G (2003) Chemical solution deposition of semiconductor films. Marcel Dekker, Inc. New York
10. Kaur I, Pandya DK, Chopra KL (1980) Growth kinetics and polymorphism of chemically deposited CdS films. *J Electrochem Soc* 127:943–948

11. Froment M, Lincot D (1995) Phase formation processes in solution at the atomic level: metal chalcogenide semiconductors. *Electrochim Acta* 40:1293–1303
12. Ó Brien P, McAleese J (1998) Developing an understanding of the processes controlling the chemical bath deposition of ZnS and CdS. *J Mater Chem* 8:2309–2314
13. Nakada T, Mizutani M (2002) 18% Efficiency Cd-free Cu(In, Ga)Se₂ thin-film solar cells fabricated using chemical bath deposition (CBD)-ZnS buffer layers. *Jpn J Appl Phys* 41:L165–L167
14. Nair MTS, Nair PK, Zingaro RA, Meyers EA (1993) Enhancement of photosensitivity in chemically deposited CdSe thin films by air annealing. *J Appl Phys* 74:1879–1884
15. Radhu S, Vijayan C (2011) Observation of red emission in wurtzite ZnS nanoparticles and the investigation of phonon modes by Raman spectroscopy. *Mater Chem Phys* 129:1132–1137
16. Beserman R, Balkanski M (1970) Vibrational properties of mixed CdS_xSe_{1-x}. *Phys Rev B* 1:608–613
17. Kandasamy K, Singh HB, Kulshreshtha SK (2009) Synthesis and characterization of CdS and CdSe nanoparticles prepared from novel intramolecularly stabilized single-source precursors. *J Chem Sci* 121:293–296
18. Loghman-Estarki MR, Hajizadeh-Oghaz M, Edris H, Razavi RS (2013) Comparative studies on synthesis of nanocrystalline Sc₂O₃-Y₂O₃ doped zirconia (SYDZ) and YSZ solid solution via modified and classic Pechini method. *Cryst Eng Comm* 15:5898–5909
19. Mohammadikish M, Davar F, Loghman-Estarki MR (2013) Low temperature preparation of 3D solid and hollow ZnS nanosphere self-assembled from nanoparticles by varying sulfur source. *J Clust Sci* 24:217–231
20. Hayek M, Brafman O (1971) In: International conference on light scattering in solids, Paris, p 76
21. Comas F, Studart N, Marques GE (2004) Optical phonons in semiconductor quantum rods. *Solid State Commun* 130:477–480
22. Lange H, Artemyev M, Woggon U, Thomsen C (2009) Geometry dependence of the phonon modes in CdSe nanorods. *Nanotechnology* 20:045705 (5pp)
23. Dzhagan VM, Lokteva I, Valakh MY, Raevska OE, Kolny-Olesiak J, Zahn DRT (2009) Spectral features above LO phonon frequency in resonant Raman scattering of small CdSe nanoparticles. *J Appl Phys* 106:084318–084318-6
24. Davar F, Loghman-Estarki MR, Ashiri R (2015) From inorganic/organic nanocomposite based on chemically hybridized CdS-TGA to pure CdS nanoparticles. *J Ind Eng Chem* 21:965–970
25. Madelung O (2004) Semiconductors data handbook. Springer, Berlin, pp 815–835
26. Ju Seo D (2004) Structural and optical properties of CdO films deposited by spray pyrolysis. *J Korean Phys Soc* 45:1575–1579
27. Jin BJ, Woo HS, Im S, Bae SH, Lee SY (2001) Relationship between photoluminescence and electrical properties of ZnO thin films grown by pulsed laser deposition. *Appl Surf Sci* 169–170:521–524
28. Riehl N (1981) Intrinsic defects and luminescence in II–VI-compounds. *J Lumin* 24–25(Part 1):335–342
29. Zeng JY (1991) Introduction to quantum mechanics. Peking University Press, Beijing
30. Wolf EL (2004) Nanophysics and Nanotechnology: An Introduction to Modern Concepts in Nanoscience, Wiley, Weinheim, p 63
31. Jiang Z, Sun H, Qin Z, Jiao X, Chen D (2012) Synthesis of novel ZnS nanocages utilizing ZIF-8 polyhedral template. *Chem Commun* 48:3620–3622